ARTICLE

Check for updates

Multilayers for directed energy accelerated lightsails

Giovanni Santi [1], Giulio Favaro[2], Alain J. Corso [3], Philip Lubin[4], Marco Bazzan [2], Roberto Ragazzoni[2,5], Denis Garoli[6] & Maria G. Pelizzo [7✉]

A lightsail accelerated via directed energy is a candidate technology to send a probe into the deep space in a time period compatible with human life. The light emitted by a ground-based large-aperture phased laser array is directed onto the lightsail to produce a thrust by transferring the momentum of the incident photons. Here we demonstrate that optimized multilayer structures allow ultralight spacecraft being accelerated by laser radiation pressure up to 20% of the light velocity, and eventually even above, as long as a compromise between efficiency and weight is achieved. Layer materials are selected to provide high reflectance in the Doppler-shifted laser wavelength range as well as high emissivity in the infrared, this last characteristic being required to survive to the temperature increase during the acceleration phase.

[1] Università di Padova, Centro di Ateneo di Studi e Attività Spaziali (CISAS), via Venezia, 15, 35131 Padova, Italy. [2] Università di Padova, Dipartimento di Fisica e Astronomia, via Marzolo 8, 35131 Padova, Italy. [3] Consiglio Nazionale delle Ricerche - Istituto di Fotonica e Nanotecnologie (CNR-IFN), via Trasea, 7, 35131 Padova, Italy. [4] Department of Physics, University of California, Santa Barbara, CA 93106, USA. [5] Istituto Nazionale di Astrofisica, Osservatorio Astronomico di Padova, Vicolo dell'Osservatorio, 5, 35122 Padova, Italy. [6] Istituto Italiano Tecnologie, Via Morego, 30, 16163 Genova, Italy. [7] Consiglio Nazionale delle Ricerche, Istituto di Elettronica, Ingegneria dell'Informazione e delle Telecomunicazioni, via Gradenigo, 6B, 35131 Padova, Italy. ✉email: pelizzo@dei.unipd.it

Space exploration is an objective of fundamental importance for the economic, social and, above all, cultural growth of the society. In the incoming years, new technologies and missions will be devoted to the exploration of the solar system and to the colonization of nearby space. On the other hand, exploration of the deep space still remains an impractical dream, mainly due to the limited propulsive means. However, more and more researchers, driven by the desire for knowledge of the universe, are orienting their activities towards the search for technological solutions. Recently, attention is paid in evaluating two possible technologies, being nuclear and laser propulsion, which in principle could allow interstellar travels. Nuclear propulsion is considered the most promising technology, even though practical and cost-effective solutions have not been identified yet. The main problems relate to the large mass of propellant involved in ground preparation, which can pose risks for human health. An alternative solution is represented by the use of a directed energy system, such as sails accelerated by the radiation pressure of a light beam.

Solar sails have been developed and tested on various missions starting from the 2010[1]; however, the isotropic power provided by the Sun is not enough to allow the acceleration needed to reach the desired relativistic velocity in the target distance, so that high power lasers are now considered as potential source of radiation. Depending on the mechanisms that generate the thrust, laser propulsion systems can be either propellant-based or propellant-less[2]: in the first case a thrust is provided by the light-driven ejection of a flux of ablated particles of non-zero rest mass[3,4], while for the second one the primary mechanism of thrust generation is due to the energy transfer from incident photons[5–9]. Moreover, a new process that generates propulsion has been recently discovered, being the Light-Induced Ejected Electrons in graphene materials[10]. An additional concept refers to the use of the laser for on-board conversion of the beamed energy into electricity used to power an electric propulsion system[11]. However, none of the techniques which are based on the ejection of material are designed to achieve relativistic speeds.

The main advantage in using the directed energy propellant-less approach is that source of energy is fully external to the spacecraft itself, so that there is no need to carry additional weight. Moreover, a ground-based laser system could be re-used to launch multiple spacecrafts, making its realization cost effective. The goal of the NASA Starlight program[12] is to enable small spacecrafts to achieve relativistic flight, in order to plan the first interstellar missions with targets including our nearest neighbor, the Alpha Centauri system[7–9]. This line of thought was subsequently continued by the Starshot Breakthrough Initiative[13]. In both the NASA Starlight and subsequent Starshot programs the spacecraft system consists of two main components: a primary spacecraft reflector, or "lightsail", propelled by a phased array laser, and a small payload, called a "wafer-scale spacecraft" or "starchip", that contains all the electronic components and sensors to gather and transmit the information. A hybrid mode of combining the spacecraft and reflector into a quasi-homogeneous structure is also conceivable. This study is agnostic to the detailed approach. As the laser flux at the spacecraft reflector is of the order of $10 - 100$ GW m^{-2} at distances from the laser of the order of the distance to the Moon, a laser phased array based is used in place of one single high powerful laser[9]. The NASA Starlight and DEEP-IN programs explored this extensively in a series of papers and laboratory demonstrations. Prototypes supporting phase locking over array diameters up to 50 km were feasible with better than 1/100 of a wave phase error achieved[12], exceeding the previous expectations. This is extremely encouraging, though a vast amount of technological development needs to be done to realize such a system. The use of phased laser array would reduce the overall complexity of the source development project, allowing the modularity needed to laboratory prototyping engineering and relative tests.

The present study assumes a scalable, modular directed energy source with emission at 1064 nm, used to accelerate a spacecraft up to a target velocity of $0.2c$; this value could be further extended depending on the requirements of the mission. Such laser wavelength has been proposed and demonstrated in the NASA Starlight program using Yb doped fiber laser amplifiers in a Master Oscillator Phased Array topology. The optimization at a selected wavelength is only one example and does not exclude any other one. Since one of the goals is to allow relativistic flight, the high-speed spacecraft will experience a longer wavelength than was initially emitted and thus two options need to be explored. One option is that the laser changes its emission wavelength to shorter ones as the spacecraft speeds up, so that the received wavelength at the spacecraft is constant; as an alternative, the reflector needs to be broadband enough to allow a modest or perhaps large dynamic range of received wavelengths. This paper focuses on the latter approach and looks at relatively broad bandwidth reflectors. It outlines the criteria to select the laser wavelength through a detailed analysis of the materials thermal properties, being generally more suitable as the wavelength increases, and modeling the ligthsail thermal evolution; vice-versa, after selecting the laser operation wavelength, the lightsail's structure should be engineered to survive to the extreme conditions arising during the acceleration phase.

In this perspective, the aim of this work is to provide a step ahead to the analysis reported by Ilic et al.[14]. In that paper, the authors demonstrated the feasibility of using ideal thin-film heterostructures as building-block elements of a laser-driven lightsail at 1200 nm, due to their ability to achieve substantial reflectance while maintaining low absorption in the near-infrared, significant emissivity in the mid-infrared, and a very low mass. They provided a minimization of a figure of merit which describes the lightsail performance as function of its structural parameters. In some cases, they have also evaluated the solution in term of their thermal stability assuming a strict thermal equilibrium. In the present work, real periodic multilayer structures undergo an optimization process at 1064 nm, by including the contribution of the lightsail's material absorption. The thermal analysis is carried on afterwords by providing an accurate description of the thermal evolution as a function of the spacecraft's velocity in nonthermal equilibrium. In doing so, we assume a set of extinction coefficient values in the Doppler-shifted wavelength region of the laser source to evaluate the dependence on the final temperature, together with different conditions of the directed energy laser power. Lightsail optimization was carried out considering a series of multilayers that include different materials. We finally discuss the impact of the laser wavelength selection in the propulsion system definition and some suitable structures to be used, which guarantee the survival of the lightsail during the acceleration phase at 1064 nm, as well as their associated manufacturing challenges.

Results and Discussion
Optimization of the multilayer lightsail. The lightsails are designed by considering a material couple arranged in a stack of N layers, as represented in Fig. 1. In this description D is the characteristic dimension of the sail and α models its specific shape, such that the sail surface is $S = \alpha D^2$.

Optimization of the lightsail requires the correct determination of the equation of motion of the object under the trust provided by the laser beam. Assuming that the laser system provides a constant beam power P_0 at all distances and settings, the power of
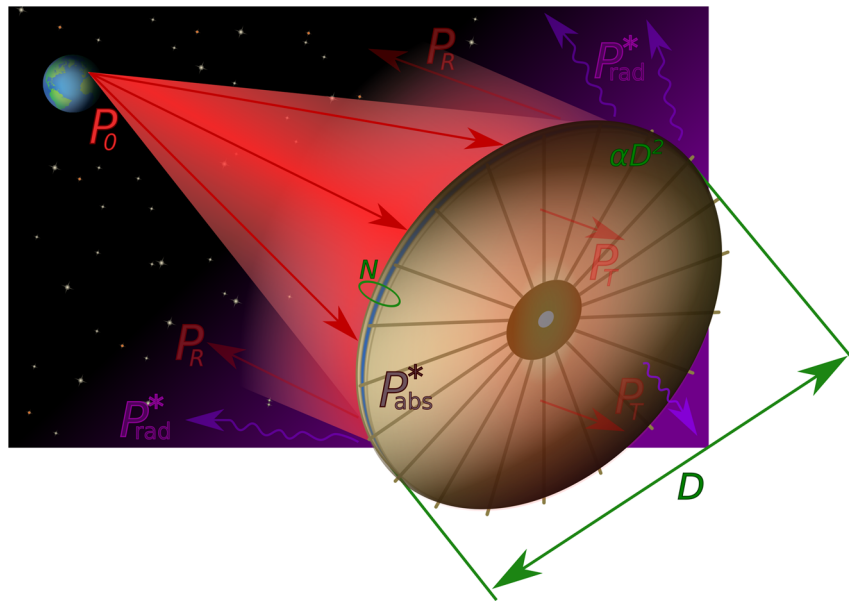
Fig. 1 Representation of the operation conditions of the multilayered lightsail. The red arrows denote the incident, transmitted and reflected laser power, while the violet ones indicate the thermal radiation leaving the structure from the front and back surfaces. The surface area is modeled as αD^2; $\alpha = 1$ for a squared lightsail of side D and $\alpha = \pi/4$ for a circular lightsail of diameter D.

the incident beam on the lightsail, as a function of the spacecraft speed $\beta = v/c$ and as seen by the reference frame from Earth, is $P_0(1 - \beta)$, where the term $(1 - \beta)$ accounts for the photon travel time between the beamer and the lightsail. Depending on the lightsail's properties, the incident power is either reflected, transmitted, or absorbed. The interaction of laser photons can be thus modeled by accounting for the optical coefficients and for the Doppler transformation of the incident power (Supplementary Note 1: LASER-thrusting theory). By introducing the reflectance R, transmittance T and absorption A, calculated at the corresponding Doppler-shifted wavelength as seen by the sail, and considering that the variation of the energy of the spacecraft is equal to the difference between the power impinging on the lightsail and that lost by transmittance and reflectance, the following differential can be obtained:

$$dt = \frac{mc^2\gamma^3}{P_0}\frac{(1 + \beta)}{(1 - \beta)}\frac{1}{[A + 2R]}d\beta; \tag{1}$$

Note that Equation (1) is formally equivalent to that obtained in[7,14,15], with the difference that the contribution for absorption is now included. The acceleration distance at the end of the acceleration phase $L(\beta_f = 0.2)$ is used to determine the point where the diffraction spot from the laser beamer is equal to the dimension of the sail[14] by integrating the instantaneous speed from 0 up to the target velocity β_f in Equation (1). By writing explicitly the mass term $m = m_s + m_p = \alpha D^2\rho_s + m_p$, where m_s is the mass of the sail, m_p the mass of the payload and ρ_s the areal density, it is then possible to derive an expression for the requirements on the laser system $P_0 d_0$, where d_0 is the diameter of the beamer. According to[7], the maximum speed occurs when $m_s = m_p$, so that:

$$P_0 d_0 = 4\lambda_0 c^3 \sqrt{m_p}\sqrt{\alpha}\int_0^{\beta_f}\frac{\sqrt{\rho_s}}{[A + 2R]}\frac{\beta\gamma}{(1 - \beta)^2}d\beta$$
$$= 4\lambda_0 c^3 \sqrt{m_p}\sqrt{\alpha} \cdot \mathrm{FOM}(\rho_s, R, A) \tag{2}$$

where the function $\mathrm{FOM}(\rho_s, R, A)$ is the Figure of Merit (FOM) to be optimized in this problem[14] in order to minimize the beamer specifications. The FOM allows, indeed, to ignore the payload mass while comparing different sail structures as it includes only

ρ_s, and at the same time poses a constraint on the characteristics of the beamer.

The materials considered for the multilayer lightsail optimization are Si, MgF_2, SiC, SiO_2, Al_2O_3, and TiO_2. These materials are in fact widely used in the realization of optical mirrors and filters for different purposes, so optical parameters are available in literature; moreover, with respect to other common materials such as ZrO_2 and Ta_2O_2, they have lower densities, which makes them more suitable candidates for the ligthsails. A genetic algorithm is applied to obtain the optimized layer thicknesses by minimizing the FOM in (2). The optical constants of the materials used for the computation of the FOM are taken from the literature[16–24] and reported in Supplementary Fig. 1 and Supplementary Fig. 2; for additional information on materials optical properties and selected spectral ranges see Supplementary Note 2. Note that while the real part of the refraction index is available for all the materials in the thin film form, the extinction coefficient barely impact on the FOM value; when not available, as in the case of Si and Al_2O_3, they have been borrowed from those determined on crystal bulks and carefully used in the thermal analysis (see Section 3); moreover, it has been verified that the real part of the refraction index of Si and Al_2O_3 in amorphous and crystal form are very similar. First, we simulate stacks which include one of the selected materials coupled with the vacuum. This allows to obtain ideal structures with a maximum optical contrast and thus upper bound performance. As a second step, different materials combinations have been considered. The optimization is carried out for different number of layers (up to 7). The obtained FOM are reported in Fig. 2a, b, respectively. Interestingly, a decreasing trend as the number of layers increases is observed in the FOM value of SiO_2, Al_2O_3, and MgF_2 based structures in Fig. 2a, being the Si-based structures the optimum ones, while an opposite behavior is observed for the real structures as reported in Fig. 2b, in which the stack is made by two different materials. In this last case, when the layer number is increased from an even number to an odd one, the FOM value is almost unchanged, even when a large number of layers are used. By looking to Table 1, where the parameters of the structures are reported, it is clear that the optimization of the even structures lead always to a last layer with a thickness of 10 nm, which has
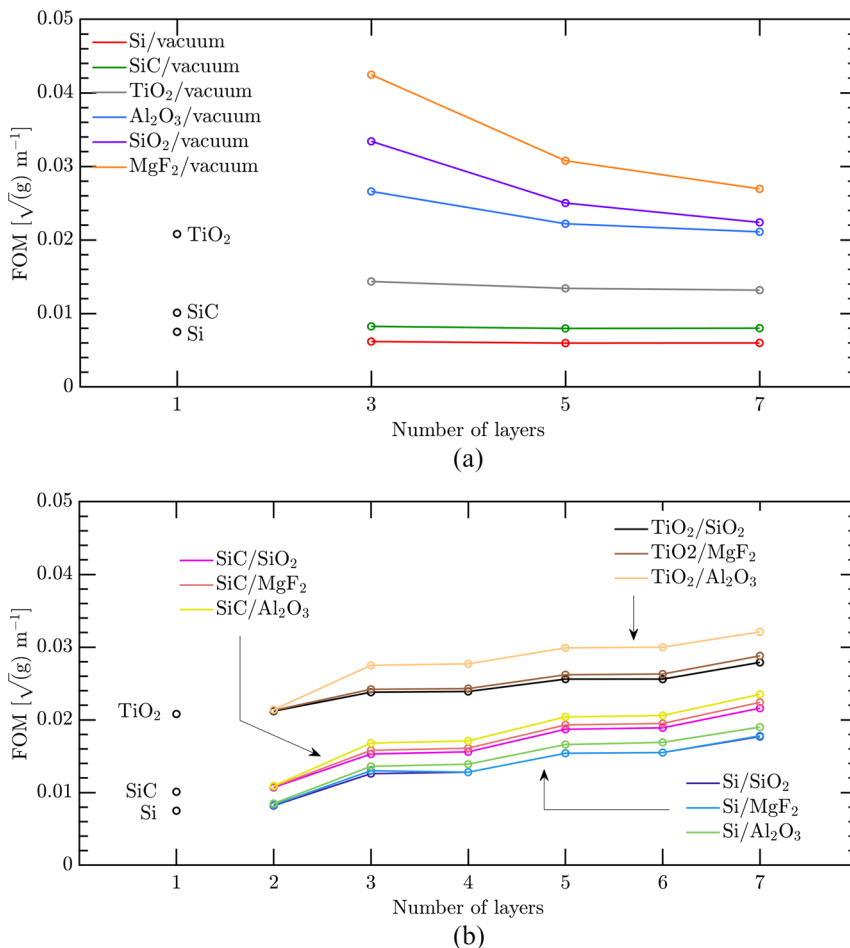
Fig. 2 Optimized FOM values from different multilayer. a structures based on material$_1$/vacuum. **b** structures based on material$_1$/material$_2$. The simulations are performed for an increase number of layers N.

Table 1 Parameters of optimized structures: volume density ρ, optimized thickness t_{opt}, area density ρ_s and FOM.

Structure	ρ [g cm^{-3}]	t_{opt} [nm]	ρ_s [g m^{-2}]	FOM [$\sqrt{g}$ m^{-1}]
Si	2.33	52	0.135	0.0074
SiC	3.24	61	0.198	0.0101
TiO$_2$	4.23	104	0.440	0.0208
Al$_2$O$_3$	3.95	157	0.6202	0.0509
SiO$_2$	2.65	181	0.480	0.0736
MgF$_2$	3.15	188	0.592	0.0965
Si/SiO$_2$	2.33/2.65	56/10	0.157	0.0082
Si/MgF$_2$	2.33/3.15	57/10	0.164	0.0083
Si/TiO$_2$	2.33/4.23	55/10	0.170	0.0085
Si/Al$_2$O$_3$	2.33/3.95	57/10	0.172	0.0085
SiC/SiO$_2$	3.24/2.65	64/10	0.234	0.0107
SiC/MgF$_2$	3.24/3.15	63/10	0.236	0.0108
SiC/Al$_2$O$_3$	3.24/3.95	63/10	0.244	0.0109
SiC/TiO$_2$	3.24/4.23	60/10	0.237	0.0108
TiO$_2$/SiO$_2$	4.23/2.65	102/10	0.458	0.0212
TiO$_2$/MgF$_2$	4.23/3.15	103/10	0.467	0.0213
TiO$_2$/Al$_2$O$_3$	4.23/3.95	101/10	0.467	0.0214
Si/SiO$_2$/Si	2.33/2.65	88/96/89	0.668	0.0126
SiC/SiO$_2$/SiC	3.24/2.65	85/142/88	0.937	0.0153
TiO$_2$/SiO$_2$/TiO$_2$	4.23/2.65	121/203/121	1.562	0.0238
Si/SiO$_2$/Si/SiO$_2$	2.33/2.65	89/97/87/10	0.694	0.0128
SiC/SiO$_2$/SiC/SiO$_2$	3.24/2.65	98/113/97/10	0.958	0.0156
TiO$_2$/SiO$_2$/TiO$_2$/SiO$_2$	4.23/2.65	121/205/117/10	1.5765	0.0239
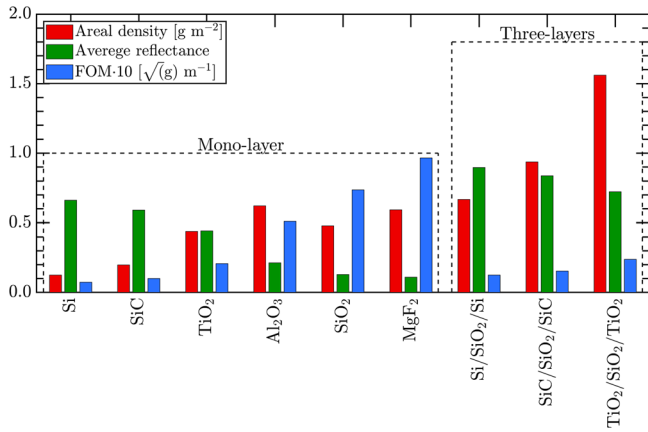
Fig. 3 Areal density, FOM and reflectance of lightsails. The areal density (red bar) and (average) the reflectance (green bar) are shown for some selected structures, as grouped by the number of layer. For each group, the value of the FOM (blue bar) increases from left to right.

been set as the minimum acceptable by the algorithm. This means that, in the even structures, the increase of the last layer thickness always degrades the FOM values. Moreover, the optimal structures are represented by the odd ones with the lower adjacent number. In particular, the structures $N = 1, 3$ have the lower FOM values, while the $N = 2, 4, 6$ are considered as a worsening case of those with $N = 1, 3, 5$ in term of propulsion efficiency, as the additional top layer always increases the FOM.

Single-layer structures with minimum FOM values are those built by materials characterized by an higher refractive index, being the case of Si, SiC, and TiO_2. These materials are thus selected as the base ones for building more complex structures. The material that in principle should be used as a second layer in a bi-layer or, more in general, in a multilayer is SiO_2, as when coupled with each of the base materials provides the best performance in term of FOM (Table 1); however, in the next section, it will be clear that even layer structure can be only slightly beneficial for the thermal stability of the lightsail, while, as said, are detrimental for the FOM.

Two parameters concur to determine the FOM value of the multilayers, i.e. the reflectance and the areal density, this last can be calculated as $\rho_s = \sum_i \rho_i t_i$, where ρ_i is the mass density of the i-th layer with thickness t_i, being the first layer eventually the substrate. In Table 1 such parameters are reported for each of the 1, 2, 3, 4-layers stack considered. Note that, for a given N, the structures having lower ρ_s are generally associated with a lower FOM value, in accordance with our analysis. In Fig. 3 the areal density, the reflectance and the FOM of selected structures are reported to allow a comparison of their performance.

The acceleration time to reach the final velocity β_f can be computed by integrating equation (1):

$$t = \frac{2\rho_s c^2}{I_0} \left[\int_0^{\beta_f} \frac{\gamma}{(1-\beta)^2 [A + 2R]} \cdot d\beta \right] = t_c \cdot \xi \quad (3)$$

In the optimal mass regime (i.e. $m_s = m_p$), in (3) m has been re-written as $m = 2 \cdot S \cdot \rho_s$, while $P_0 = S \cdot I_0$. Consequently, the equation is independent on the sail surface area, while it depends on the irradiance I_0. In (8), t results as a product of two terms, the characteristic time of the system $t_c = \frac{2\rho_s c^2}{I_0}$ and the dimensionless term ξ that takes into account the relativistic efficiency of the lightsail. The second term, ξ, depends on the optical properties of the lightsail and it reaches its minimum value of 0.1261 in the case of a perfectly reflective lightsail (i.e. $R = 1$ and $A = 0$ at all velocities). Note that the equation (3) is formally equivalent to the
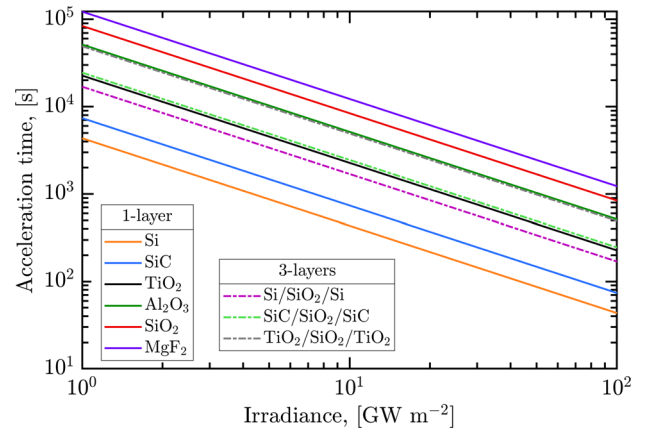
Fig. 4 Lightsail acceleration time versus laser irradiance. The acceleration time to reach β_f in the beamer reference frame is shown for the lightsail structures considered in this study.

one provided by Kulkarni et al.[8], except for the fact that in this case the lightsail is not a perfect reflector.

Figure 4 shows the acceleration time in the beamer reference frame for the 1- and 3- layer lightsail structures considered in this study. As expected, the minimum time is associated to the Si-based structures, which have the minimum FOM values, while the higher value are for the TiO_2-based structures. Given an irradiance I_0, structures with lower ρ_s have also a smaller characteristic time. However, given a payload of mass m_p, the ratio m_p/ρ_s determines the lightsail's area S, so that structures having lower areal density imply lightsails of larger size. For example, a payload of 1 g requires a sail of $S \approx 1.5 \, m^2$ in the case of the $Si/SiO_2/Si$ structure, while only of $S \approx 0.6$ for the $TiO_2/SiO_2/TiO_2$ one. We can conclude that couples with high optical contrast result in thinner layers, with a diminishing of the areal density, and ultimately an increasing of the propulsion efficiency. By looking at the results obtained so far, it appears that the optimum solutions are given by the single layer of Si (target velocity achieved after 4336 s for $I_0 = 1$ GW, 433 s for $I_0 = 10$ GW, 43 s for $I_0 = 100$ GW) and SiC (target velocity achieved after 7372 s for $I_0 = 1$ GW, 737 s for $I_0 = 10$ GW, 74 s for $I_0 = 100$ GW). However, in the next section the analysis carried out on the thermal stability of such structures will demonstrate their instability, and prove that the TiO_2 based structures are those to be further considered. With a single-layer structure, the target velocity is achieved in 22658 s for $I_0 = 1$ GW, 2266 s for $I_0 = 10$ GW, 227 s for $I_0 = 100$ GW, while with the $TiO_2/SiO_2/TiO_2$ in 49122 s, 4912 s, and 491 s, respectively.

Thermal stability of the lightsail. The thermal analysis of the lightsail is of upmost importance to understand whether the chosen structure will survive the acceleration process. Energy flows inside the system through the absorbed power and it leaves the system via the radiated power. The absorbed power in the sailcraft reference frame (identified by an *) can be expressed as:

$$P_{abs}^* = I_0 S \frac{1-\beta}{1+\beta} A(\lambda_0, \beta) \quad (4)$$

Since the lightsail is a pure passive device, the emitted power P_{rad}^* is modeled by means of thermal radiation theory:

$$P_{rad}^* = S \cdot \int_\lambda \varepsilon_\lambda(T^*, \lambda) \cdot E_{b,\lambda}(T^*, \lambda) d\lambda \quad (5)$$

being ε_λ the spectral hemispherical emissivity and $E_{b,\lambda}$ the spectral blackbody emittance. The spectral hemispherical emissivity is computed as the sum of the front and back emissivities, i.e. the emissivities associated with the front and back surfaces. The net

power is computed by the difference between the absorbed and radiated ones from equations (4) and (5) respectively. Differently from previous analysis[14], the temperature is then calculated using the thermal energy absorbed in the system in non-equilibrium conditions. Results will be remarkably important to assess the thermal evolution and stability of the ligthsail.

The time-dependent temperature evolution is obtained though numerical calculations based on the following non-linear non-homogeneous equation:

$$\frac{\partial T^*}{\partial t^*} = \frac{P^*_{\text{abs}} - P^*_{\text{rad}}}{C_{\text{sail}}} \qquad (6)$$

where $C_{\text{sail}} = \sum_i m_i c_i$ is the heat capacity of the lightsail as given by the sum of the contribution of the i-th thin film of mass m_i and specific heat capacity c_i. In our calculation, we have taken into account the dependence of C_{sail} by the temperature through β. By operating the change of variable $t^* = t\gamma^{-1}$, which relates the proper time of the beamer with the one of the sail, in (1), dt^* can be express in term of $d\beta$:

$$dt^* = \frac{2\rho_s c^2 \gamma}{I_0}\left[\frac{(1+\beta)}{(1-\beta)}\frac{\gamma}{[A+2R]} - \beta\left(\int_0^\beta \frac{\gamma(y)}{(1-y)^2}\frac{1}{A+2R}\,dy\right)\right]d\beta$$
$$(7)$$

The right term of (6) linearly depends on the area of the lightsail S through the net power $P^*_{\text{abs}} - P^*_{\text{rad}}$; at the same time, the heat capacitance scales linearly with the area through the system mass m, so that $C_{\text{sail}} = 2 \cdot S \cdot \sum_i \rho_i t_i c_i$; hence, the thermal balance of the lightsail is independent on its surface area. The acceleration and the thermal evolution of the system thus depend only on the irradiance I_0.

At each integration step $d\beta$, the dt^* retrieved by equation (7) is used to calculate the difference between the absorbed and emitted power in order to determine the temperature increment for subsequent iterations. To perform such computation, a precise knowledge of the refractive index of the involved materials is required. While the real part is generally well known, the extinction coefficient is barely available in the full spectral range needed to make the thermal analysis and, when available, this is typically known with low accuracy. Therefore, while emittance calculations are performed assuming tabulated k in the range $\lambda = 1.5 - 50\,\mu m$, which includes a ~97% of the power emitted by a body at 300 K and a ~89% of a body at 1500 K (see Supplementary Fig. 3), for the absorbed power in the laser Doppler range $\lambda = 1 - 1.225\,\mu m$ different values for the extinction coefficient have been considered, as these are critical for the thermal balance. In Supplementary Figs. 2 and 3 some available k data from literature used in the simulation are reported. Dielectric materials such as TiO_2 and SiO_2 are high-temperature low-loss transparent materials, so that they can sustain higher temperatures more easily. In turn, semiconductor material such as Si and SiC can easily achieve extinction coefficient values of the order of $10^{-9} - 10^{-10}$ above the band-gap, but the value at the band-gap is temperature dependent and the absorption rapidly increases with the temperature. This can be a major issue if the band-gap falls in the Doppler-shifted wavelength range of the incident laser radiation. SiC has a very high absorption at 1064 nm and simulations show that this leads to a thermal instability of the lightsail even for low irradiance I_0 values, so that structures including this material have been discarded. In the case of Si, the experimental values of k, largely reported in the literature, decrease as the wavelength increase[21,25]. Unfortunately, the 1064 nm laser wavelength still falls within the absorption gap of the Si, so that it is foreseen that also this materials will not perform well in term of thermal stability. To prove so, a linear fit of the k data reported in the Supplementary Fig. 3 have been used in order to

obtain values at each proper Doppler λ, each of which correspondent to a β along the acceleration phase, to be included in thermal evolution simulations. Moreover, values scaled of one and two decades have been also used in simulations. For SiO_2 and TiO_2 the simulations assumed k values reported in literature, which are 10^{-7} [16] and $6 \cdot 10^{-5}$ [23] respectively, being these constants over the whole Doppler-shifted spectral range. However, simulations have been performed using even more optimistic values, as it is reasonable to assume that lower k can be achieved by engineering such materials.

Thermal evolution of selected stacks as function of β are reported in Fig. 5, for the case of irradiance $I_0 = 1\,\text{GW m}^{-2}$ and initial temperature $T = 50\,\text{K}$. These values can resemble the case in which the lightsail is accelerated from outside the atmosphere. While the most performing solution in term of FOM is the Si single layer, this actually results thermally unstable even for very low k values (Fig. 5a). On the contrary, the TiO_2 single layer shows remarkable thermal stability for low k values (Fig. 5b). Simulations have been performed also in order to verify if a TiO_2 capping layer deposited on a Si layer can stabilize the sail; results show that this is the case only for the lower silicon k values. For this reason, structures based on Si are not further investigated. On the contrary, TiO_2 coupled with SiO_2 structures have been deeply analyzed. The use of a multilayer in place of a single layer can offer some advantages in term of the maximum temperature achieved, which decreases if 3 (Fig. 5c) or more layers are used, but only for high k value of TiO_2 (Fig. 6). However, as the number of layers increases, the FOM increases too, so that it is not convenient to use more than 3 layers, unless the total thickness of the structure matters in term of mechanical stability. In fact, while the single-layer thickness is of only 104 nm and the three layers one is of 445 nm, the seven layers one reaches about 1.1 μm.

The results obtained so far highlight the role of TiO_2 in the thermal re-emission, which derives from the high values of k that characterized it over the whole IR range considered up to 50 μm. It is worth to note that the starting temperature does not affect the thermal evolution of the structure. As an example, in Fig. 7 the case of a single TiO_2 layer with a $T_0 = 300\,\text{K}$ is reported to envision the scenario in which the ligthsail is accelerated from ground. Clearly, the final temperature reached by the lightsail is the same of that reached with $T_0 = 50\,\text{K}$, thus being independent from the starting one. Note that the TiO_2-based structures are also able to withstand an irradiance of $I_0 = 10\,\text{GW m}^{-2}$ (Fig. 8) and even $I_0 = 100\,\text{GW m}^{-2}$ (Fig. 9), as long as the extinction coefficient does not exceed 10^{-7} and 10^{-8} respectively.

Fabrication challenges. While the optimization of the FOM provides the structure which best performs in term of efficiency, the thermal analysis lastly states the feasibility of the experiment. In fact, from the results obtained in the previous sections assuming the use of a 1064 nm laser source, the most suitable structures to be adopted are not the best in term of efficiency, but those capable to survive the journey, in particular those involving TiO_2 layers. However, to achieve such a challenging outcome, a major effort is needed to engineer the material in order to reduce the k in the laser Doppler wavelength range in order to allow the use of powers up to 10 GW and eventually 100 GW, with consequent reduction of the acceleration times, shortening to 2266 and 227 s respectively. In addition, as the absorption coefficient of Si decreases at long wavelengths, the use of an operating wavelength above 1064 nm could be an advantage in terms of lightsail thermal stability and overall for the efficiency of the propulsion system. For example, the use of Yb-Er laser at 1.3 μm could guarantee higher lightsail performance, still combined with good transmittance in the atmosphere H-band.
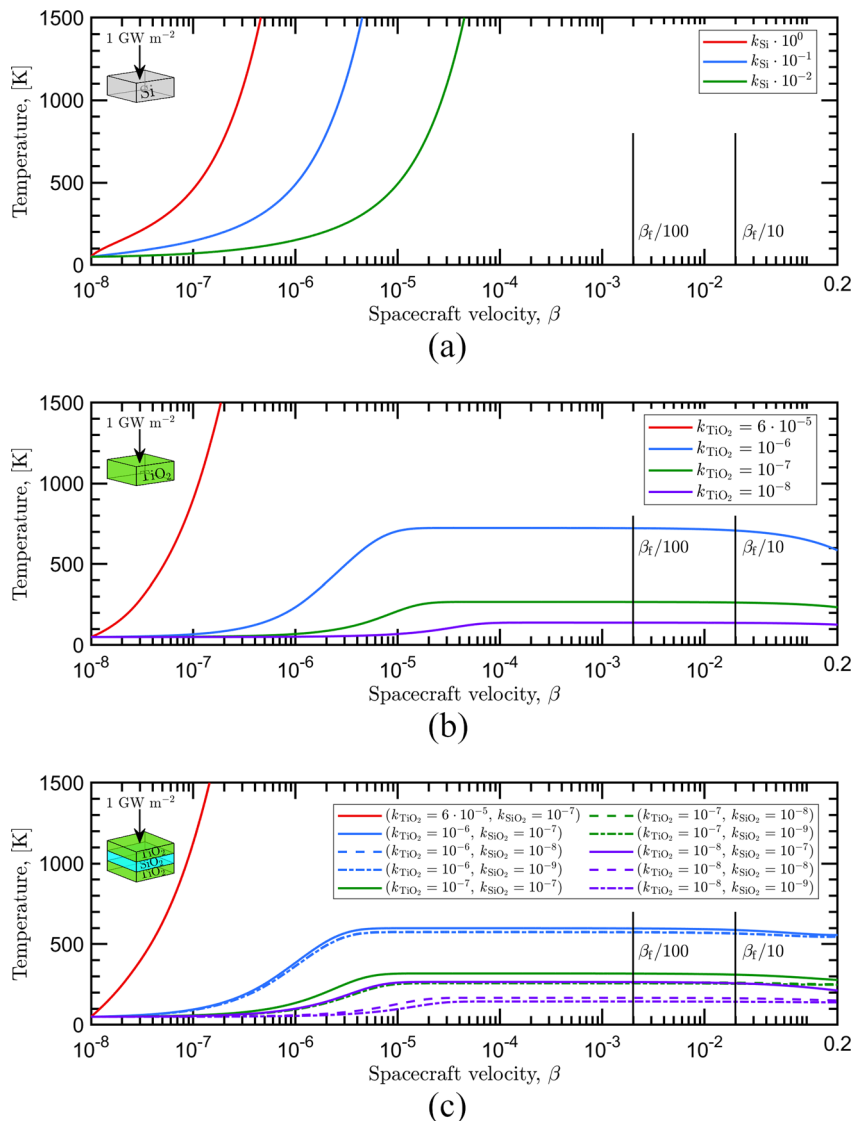
Fig. 5 Lightsail temperature evolution during the acceleration phase with a laser irradiance $I_0 = 1$ GW m^{-2}. The acceleration phase of the Si single layer is shown in (**a**), of TiO$_2$ single layers in (**b**), and of TiO$_2$/SiO$_2$/TiO$_2$ tri-layer in (**c**). The temperature evolution is reported by considering different value combinations of the materials extinction coefficient. Here the starting temperature $T_0 = 50$ K and the laser irradiance is $I_0 = 1$ GW m^{-2}.

In addition to the theoretical analysis and possible lightsails design presented in previous sections, some practical considerations should be taken into account in relation of some of the most critical aspects of such an ambitious project. In particular, the extreme constrains on the mass requires all materials to be in thin-film form. Therefore, the use of a thick substrate has to be excluded, while the self-standing solution represents the optimum technology, which can better resemble the results obtained with our simulations. However, this can pose some questions on the manufacturing process and mechanical stability, the last being discussed in the following. As an alternative, membranes could be used as substrates. High-performance, lightweight, and flexible materials that can meet the high-temperature requirements have been recently proposed. For example, fabrication of 44 mg cm^{-3} [26] and even 27.34 mg cm^{-3} [27] substrates have been reported, with the possibility of peeling transparent single-layers fibrous membranes. The extremely low density is achieved by electro-spinning, which allows to obtain a very high porosity of the substrate membrane. The typical applications for such membranes are efficient heat insulation, acoustic absorption, water purification, and many others[28]; moreover, they share many of the characteristics that are

desirable for our lightsails and represent a promising solution that needs further investigations. In particular, the effect of the membrane on the efficiency should be evaluated. On the good side, deposition of thin-film multilayers with meters scale area is already feasible by using physical vapor deposition processes.

In both cases in which the sail is in the free-standing form or sustained with highly porous membranes, the mechanical stability of the sail upon large thermal gradients is directly linked to the stress arising into the film. A single TiO$_2$ layer sail in free-standing form is stress-less by itself. In contrast, in a multilayer coating structure, the total stress is the function of the layers thickness and the stress at each interface, which can be calculated according to the following formula:

$$\sigma_{tot} = \frac{\sum_{i=1}^{N} \sigma_i d_i}{\sum_{i=1}^{N} d_i} \qquad (8)$$

where σ_i and d_i are the stress and thickness of the i-th layer, N is the maximum number of layers. Considering the room temperature T_{amb} as the rest temperature, each layer undergoes
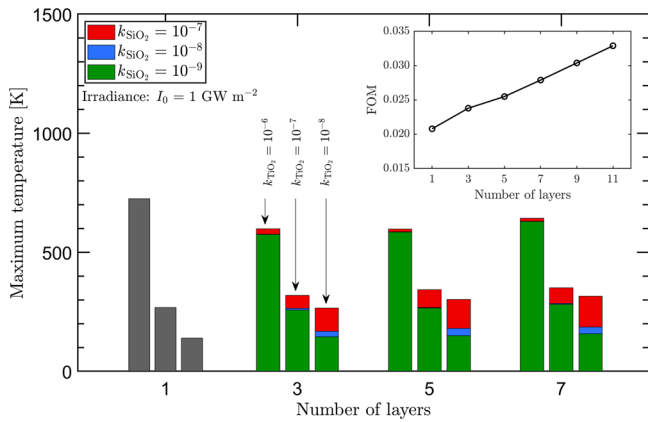
Fig. 6 Maximum temperature reached during the acceleration phase. The temperature is provided for the TiO_2-based lightsails with SiO_2 as low-index material, for different values of extinction coefficients. In the inset the FOM is reported for increasing number of layers.
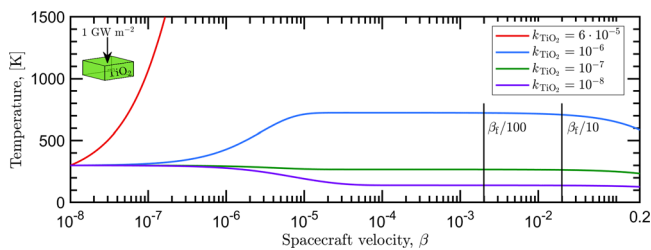
Fig. 7 TiO_2 single layer lightsail temperature evolution during the acceleration phase with initial temperature at $T_0 = 300$ K. The temperature evolution is calculated for different values of the extinction coefficients. Here the irradiance is $I_0 = 1$ GW m^{-2}.

a stress σ_i[29,30]:

$$\sigma_i = Y_i \alpha_i (T_X - T_{amb}) + \sigma_i^{Btin} \qquad (9)$$

where Y_i and α_i are the Young's modulus and the expansion coefficient of the i-th layer material respectively, T_X is the limit lightsail working temperature (e.g. the maximum or the minimum temperature at which it can operate) and σ_i^{Btin} is the built-in stress of the i-th layer at room temperature, i.e.the intrinsic stress the film growths with. Luckely, SiO_2 layers usually show a built-in compressive stress, whereas TiO_2 layers show a built-in tensile stress[31], so that they act in compensation when the SiO_2/TiO_2 multilayer is deposited. Moreover, by depositing the structure at a specific temperature or treating it with postdeposition annealing cycles, the total built-in stress can be reduced to values lower than 5 MPa[30]. Thermal gradients produce additional stress that adds to the built-in stress. By adopting the value of Young's modulus and the expansion coefficient reported in Table 2, calculations show that the SiO_2/TiO_2 tri-layer structure suffers a stress of $\simeq -153$ MPa (compressive) and $\simeq +400$ MPa (tensile) when the temperature drops to 50 K or rises to 700 K, respectively. Such values are not critical to induce a fatal damage, such as layer delamination or coating cracking: previous tests carried out for applications in nuclear fusion have proven that SiO_2/TiO_2 dielectric coatings remain stable for thermal cycles up to $\simeq 624$ K tests for over 1 h. Moreover, after 85 h annealing at $\simeq 694$ K samples reveals only a slight reduction of the optical performance, mainly due to the formation of crystalline phases in the multilayer, and to some surface defects related to small local delamination[32].

Assuming a purely elastic strain in the structure, the total stress accumulated with temperature can induce local or global sail bending. The radius of curvature induced by the bending in a free-standing structure is in the 10 m-scale. The solution that includes the substrate in place of the free-standing one offers the advantage that sail bending is reduced, also in the case of the TiO_2 single layer, which when coupled with the support can impress a tensile stress up to $\simeq 170$ MPa.

Another aspect to be considered is the mechanical strength of the multilayer structure. There is very little information in the literature on the mechanical properties of thin films[33], though we can derive some general conclusions. To avoid a mechanical failure, the pressure acting on the lightsail must verify the condition:

$$P < (\sigma_{UTS} \cdot t)/D \qquad (10)$$

where σ_{UTS} is the ultimate tensile strength of the sail material and t its thickness. The instantaneous pressure P can be expressed by normalizing the force acting on the lightsail to its surface:

$$P = \frac{I_0}{c} \frac{1-\beta}{1+\beta}[(1+\beta)A + 2R] \qquad (11)$$

Figure 10 shows the maximum pressure experienced during acceleration by different TiO_2/SiO_2 -based multilayer lightsails, being the number of layers in the range between 1 and 7. In the most critical case of an irradiance of $I_0 = 100$ GW/m^2, the maximum pressure experienced increases from 308 Pa (single layer) up to 620 Pa (7-layers). Using Eq. (10), such values correspond to a maximum ratio σ_{UTS}/D of 2.96 GPa m^{-1} for the single layer and 284 MPa m^{-1} for the 7-layers structure respectively. While at our knowledge the σ_{UTS} for TiO_2 is not available, and more in general very limited information are available for amorphous materials, the silica glass has tensile strength >5 GPa[34]. Taken into account such value, large areas can be fabricated when the number of layer is above 3, while the system needs to be carefully assessed in the case of a single layer. Again, as the FOM increases with the number of layers, the acceleration time increases to 4912 s and 491 s for a $N = 3$ structure for powers of 10 GW and 100 GW respectively.

Another issue regards the stability attitude of lightsail during the acceleration phase, as small perturbations can cause the light sail losing its alignment with respect to the laser beam axis. This can be induced by many factors, including disturbances at the source or at the sail, but also by imperfections in the sail manufacturing. Such misalignment can result in a complete failure of the system, due to the impossibility to recover its orientation relative to the beam axis. The potential stability of conical-shaped sails riding on a Gaussian beam have been deeply analyzed[35,36]. A solution based on a spherical sail coupled with a multimodal laser beam profile has been proven through numerical simulations to be capable to re-orient itself without active feedback[37]. Another solution to be considered is the use of a diffraction grating surface, which is stable to small perturbations[38]. The thin films presented in this work could be used to functionalize such shaped or patterned substrates. Another class of stable lightsail solutions under study is based on the use of nanophotonic structures and metasurfaces[39–45]. While these solutions can offer high performance in terms of efficiency and stability, the effective scalability of the technology over large surface areas needs to be further investigated. One of the advantages of the solution proposed in this work is its feasibility, as coatings are commonly deposited on mirrors for telescopes even of meters size. Another advantage consists in the relative dependence of the reflectance from the laser impinging angle; in fact, the layers thicknesses are not binded to the Quarter Wave Optical Thickness condition, so that the reflectance curve is
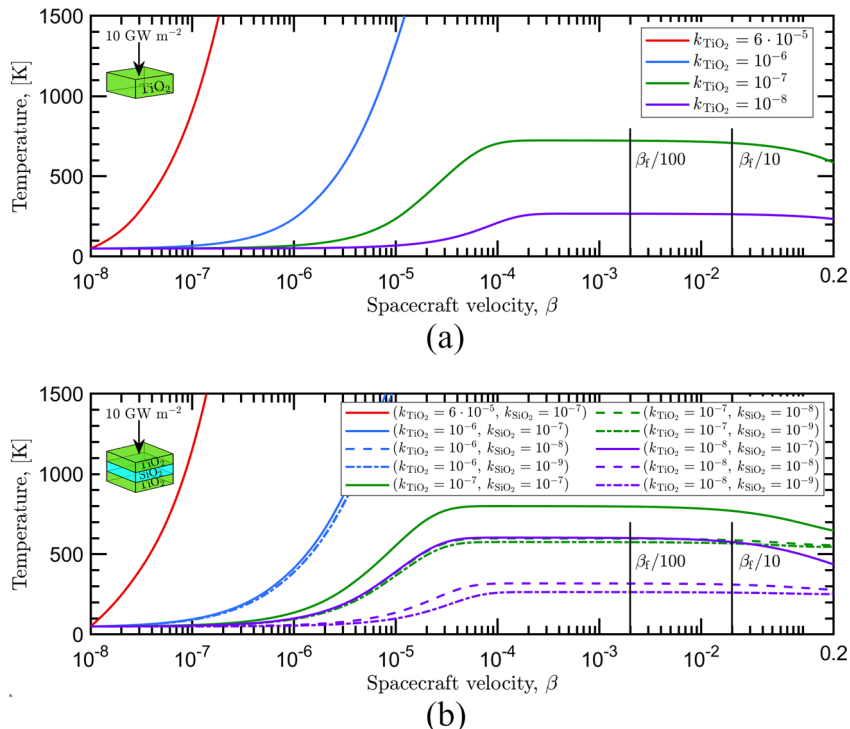
Fig. 8 TiO₂-based lightsail temperature evolution during the acceleration phase with a laser irradiance $I_0 = 10$ GW m^{-2}. The temperature evolution is calculated for the TiO₂ monolayer (**a**) and for the TiO₂/SiO₂/TiO₂ tri-layer (**b**) lightsails for different values of the extinction coefficients, given a starting temperature $T_0 = 50$ K.
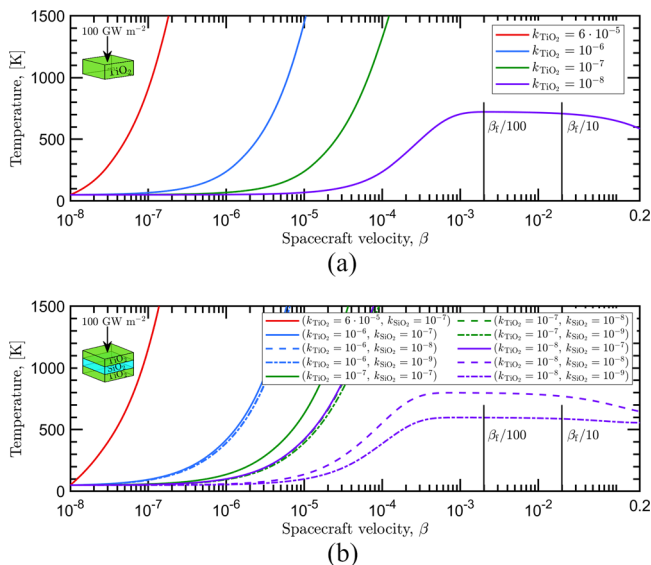
Fig. 9 TiO₂-based lightsail temperature evolution during the acceleration phase with a laser irradiance $I_0 = 100$ GW m^{-2}. The temperature evolution is calculated for the TiO₂ monolayer (**a**) and for the TiO₂/SiO₂/TiO₂ tri-layer (**b**) lightsails for different values of the extinction coefficients, given a starting temperature $T_0 = 50$ K.

not narrowband and sharply peaked at a central wavelength, as in the case of a multilayer structures made by many Quarter Wave Optical Thickness layers. The propulsion efficiency is thus only slightly affected by a change of the incidence angle, so that curve substrates can be adopted. Simulations show a variation of only 6% of the FOM for an incidence angle of 30°. In particular, for TiO₂ single layer, the merit function actually diminishes due to an increment of the reflectance with the increased angle. In case of a

shaped symmetric lighsail, this could result in a higher radiation pressure at the border of the sail with respect to the center, which should favor an increase in its stability properties.

Lastly, in case the sail must need to survive along the entire journey, for instance to be used for communication purposes, the space environmental effects have to be taken into account. In fact, the spacecraft would experience the interaction with interstellar gas and dust in the interstellar medium. Most of the it consists of gaseous matter, approximately 99% of the total mass, while the remaining part is composed of granular dust. Of the gaseous matter, approximately 98% consists of hydrogen (70%) and helium (28%), and the remaining 2% includes heavier elements such as carbon, oxygen and iron[46,47]. A theoretical study has been carried out to investigate the damage induced by various agents during a relativistic journey[48]; nevertheless the gas accumulation effect in materials that propagate at relativistic speed is still rather unexplored[49,50]. Depending on energy, ions are expected to implant at different depth in the materials, potentially causing serious damages in the lightsail. A collection of experiments carried out on virgin and protected mirrors have been reported[51–57], even though much work still needs to be done to model and prove lightsail hardness.

Conclusions

Thin-film multilayers in the sub-micrometric scale could be a valuable solution for realizing low mass direct energy accelerated lightsails. Different optimized structures have been proposed to maximize the propulsion efficiency, which depends on the reflectance and absorption of the ligthsail in the Doppler-shifted wavelength region of the laser source, and on the areal density of the lightsail itself. The proposed solutions have been analyzed in order to verify their thermal stability during the acceleration phase, which results as the ultimate criteria to assess their suitability. The most promising structures to be used with a 1064 nm laser source result to be the TiO₂-based ones, in the form of single

Table 2 Mechanical and thermal paramiters of the SiO$_2$ and TiO$_2$ materials.

Material	Young's Modulus (GPa)	Expansion coefficient (10^{-6} K^{-1})	Reference
SiO$_2$	72.5	0.24–0.55	[65]
TiO$_2$	150	10.2	[66]
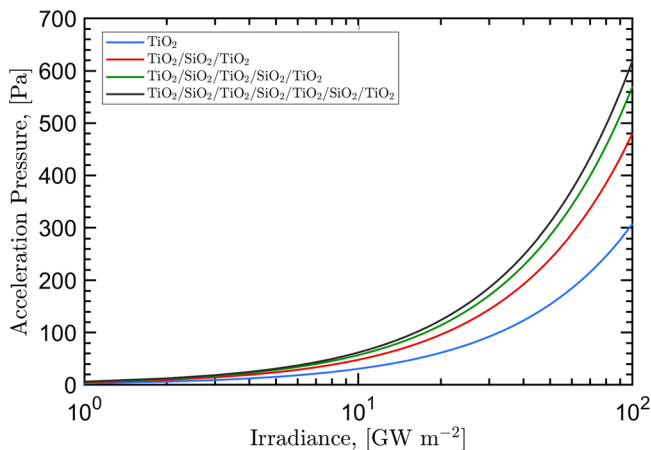
Fig. 10 Maximum acceleration pressure undergone by TiO$_2$-based lightsails. The maximum acceleration pressure to reach β_f in the beamer reference frame for the TiO$_2$-based lightsail structures have been computed for different laser irradiances.

layer or multilayer stack which include the SiO$_2$ as a second material. In term of propulsion efficiency, the single layer results to be the most performing, while the multilayers offer some advantages in term of thermal control and stiffness. The engineering process is fundamental to obtain proper optical characteristics, thus reducing the absorption of the lightsail in the Doppler-shifted wavelength of the laser in order to allow the use of high-power laser up to 100 GW. The use of a longer wavelength laser source could expand the choice of potential materials having the required optical characteristics.

Methods

Multilayer stack design. The lightsails are designed by considering a pair of materials and arranging them in a stack of N layers. The optimization of the layer thicknesses is performed by using a genetic algorithm written as a MATLAB script. This algorithm identifies the best-performing multilayer structure among a population of 50 different solutions that evolves through random variation of the layer thicknesses. The optimization uses the quarter-wave stack tuned at the wavelength in the middle of the Doppler-shift range as seeding structure. The starting solution population is generated by randomly varying the seeding structure layer thicknesses adding a quantity described by a normal distribution with a $\sigma = 20$ nm. The FOM of each solution is computed, by using the material density values reported in Table 1, and computing the reflectance and the absorbance by using the n and k values reported in Supplementary Fig. 1 and Supplementary Fig. 2, respectively. In particular, the reflectance is calculated using a transfer matrix method[58]. The algorithm runs by continuously varying the thicknesses of the population, at each step selecting the top 25 best-performing structures in term of FOM. The optimization process stops when the FOM value changes of less than 0.01% in the last 20 cycles.

Temperature evolution of the multilayer lightsail. The temperature evolution during the acceleration phase is computed by using a MATLAB script. The computation of the temperature was performed for 10001 different β values in the range from 10^{-8} to $\beta_f = 0.2$, operating either a logarithmic spacing when the incremental steps $\Delta\beta$ were shorter than 10^{-6} or a linear spacing otherwise. The computation considers a temperature starting value T_0 (i.e. 50 K or 300 K in the present study) and an initial $\beta_0 = 10^{-8}$. Eq. (4) and (5) allow to compute the absorbed and irradiated powers, while by discretizing the equation (7) the value Δt^*

is retrieved and used in (6) to compute ΔT^*. At a generic i-th computational step, the new temperature is given by $T_i^* = T_{(i-1)}^* + \Delta T_i^*$. When ΔT_i^* is calculated, this is initially computed by using the $C_{\text{sail}}(T_{(i-1)})$ value. However, the heat capacity C_{sail} is not constant, but changes with temperature. Specific heat capacity values at different temperatures have been retrieved using Comsol Multiphysics[59] and related references for the selected materials, being[60–62] for SiO$_2$[63,64], for Si and[64] for TiO$_2$. In order to take into account the C_{sail} dependence on T^* and to avoid computational instabilities, T_i^* is refined at each step using a fine computation of ΔT_i^*. ΔT_i^* is in fact finely discretized in N values, for each of which $C(T_n)$ is computed and T_i^* still derived using (6). The final value of T_i^* is then obtained by iterating the fine process over N.

Data availability
Source data for figures are referenced within the paper; simulated data are available upon request to the corresponding author.

Code availability
Code used to optimize and simulate the lightsail structure are available upon request to the corresponding author.

References
1. Tsuda, Y. et al. Flight status of ikaros deep space solar sail demonstrator. *Acta Astronaut.* **69**, 833–840 (2011).
2. Levchenko, I., Bazaka, K., Mazouffre, S. & Xu, S. Prospects and physical mechanisms for photonic space propulsion. *Nat. Photo.* **12**, 649–657 (2018).
3. Felicetti, L. & Santoni, F. Nanosatellite swarm missions in low earth orbit using laser propulsion. *Aerosp. Sci. Technol.* **27**, 179–187 (2013).
4. Phipps, C. et al. Review: Laser-ablation propulsion. *J. Propuls. Power* **26**, 609–637 (2010).
5. Marx, G. Interstellar vehicle propelled by terrestrial laser beam. *Nature* **211**, 22–23 (1966).
6. Forward, R. L. Roundtrip interstellar travel using laser-pushed lightsails. *J. Spacecr. Rockets* **21**, 187–195 (1984).
7. Lubin, P. A roadmap to interstellar flight. *JBIS - J. Br. Interplanet. Soc.* **69**, 40–72 (2016).
8. Kulkarni, N., Lubin, P. & Zhang, Q. Relativistic spacecraft propelled by directed energy. *Astronomical J.* **155**, 155 (2018).
9. Lubin, P. & Hettel, W. The path to interstellar flight. *Acta Futura.* **12**, 9–44 (2020).
10. Zhang, T. et al. Macroscopic and direct light propulsion of bulk graphene material. *Nat. Photo.* **9**, 471–476 (2015).
11. Sheerin, T. F., Petro, E., Winters, K., Lozano, P. & Lubin, P. Fast solar system transportation with electric propulsion powered by directed energy. *Acta Astronaut.* **179**, 78–87 (2021).
12. Starlight. Starlight. https://www.deepspace.ucsb.edu/projects/starlight (2021).
13. Brekthrough starshot. Breakthrough Initiatives. https://breakthroughinitiatives.org/initiative/3 (2021).
14. Ilic, O., Went, C. M. & Atwater, H. A. Nanophotonic heterostructures for efficient propulsion and radiative cooling of relativistic light sails. *Nano Lett.* **18**, 5583–5589 (2018).
15. Atwater, H. A. et al. Materials challenges for the starshot lightsail. *Nat. Mater.* **17**, 861–867 (2018).
16. Kitamura, R., Pilon, L. & Jonasz, M. Optical constants of silica glass from extreme ultraviolet to far infrared at near room temperature. *Appl. Opt.* **46**, 8118–8133 (2007).
17. Boidin, R., Halenkovič, T., Nazabal, V., Beneš, L. & Němec, P. Pulsed laser deposited alumina thin films. *Ceram. Int.* **42**, 1177–1182 (2016).
18. Siefke, T. et al. Materials pushing the application limits of wire grid polarizers further into the deep ultraviolet spectral range. *Adv. Opt. Mater.* **4**, 1780–1786 (2016).
19. Larruquert, J. I. et al. Self-consistent optical constants of sic thin films. *J. Opt. Soc. Am. A* **28**, 2340–2345 (2011).
20. Pierce, D. T. & Spicer, W. E. Electronic structure of amorphous si from photoemission and optical studies. *Phys. Rev. B* **5**, 3017–3029 (1972).
21. Green, M. A. Self-consistent optical parameters of intrinsic silicon at 300k including temperature coefficients. *Sol. Energy Mater. Sol. Cells* **92**, 1305–1310 (2008).
22. Rodríguez-de Marcos, L. V., Larruquert, J. I., Méndez, J. A. & Aznárez, J. A. Self-consistent optical constants of MgF$_2$, LaF$_3$, and CeF$_3$ films. *Opt. Mater. Express* **7**, 989 (2017).

23. Yao, J. et al. Laser-induced damage of TiO_2/SiO_2 high reflector at 1064 nm. *J. Appl. Phys.* **103**, 83–103 (2008).

24. Querry, M. R. Optical constants. Missouri Univ-Kansas City. (1985).

25. Schinke, C. et al. Uncertainty analysis for the coefficient of band-to-band absorption of crystalline silicon. *AIP Adv.* **5**, 067168 (2015).

26. Xie, Y. et al. High temperature and high strength $Y_2Zr_2O_7$ flexible fibrous membrane for efficient heat insulation and acoustic absorption. *Chem. Eng. J.* **416**, 128994 (2021).

27. Xie, Y. et al. Lightweight, high-strength, flexible YAG fibrous membrane for efficient heat insulation. *J. Alloys Compd.* **876**, 159978 (2021).

28. Burger, C., Hsiao, B. S. & Chu, B. Nanofibrous materials and their applications. *Annu. Rev. Mater. Res.* **36**, 333–368 (2006).

29. Oliver, J. et al. Stress compensation in hafnia/silica optical coatings by inclusion of alumina layers. *Opt. Express* **20**, 16596–16610 (2012).

30. Guo, C. & Kong, M. Fabrication of ultralow stress TiO_2/SiO_2 optical coatings by plasma ion-assisted deposition. *Coatings* **10**, 720 (2020).

31. Sankur, H. & Gunning, W. Sorbed water and intrinsic stress in composite TiO_2-SiO_2 films. *J. Appl. Phys.* **66**, 807–812 (1989).

32. Krimmer, A. et al. Testing of a SiO_2/TiO_2 mirror coating on a stainless steel substrate under iter in-port conditions. *Fusion Eng. Des.* **96**, 817–820 (2015).

33. Saunders, S. & Vetters, H. Standardisation of test methods for the mechanical properties of thin coatings. *Thin Solid Films* **299**, 82–87 (1997).

34. Glaesemann, G. S. Optical fiber mechanical reliability. *White Paper* **8002**, 1–62 (2017).

35. Popova, E., Efendiev, M. & Gabitov, I. On the stability of a space vehicle riding on an intense laser beam. *Math. Methods Appl. Sci.* **40**, 1346–1354 (2017).

36. Shirin, A. et al. Modeling and stability of a laser beam-driven sail. *Am. Control Conf.* **6**, 4269–4275 (2021).

37. Manchester, Z. & Loeb, A. Stability of a light sail riding on a laser beam. *Astrophys. J. Lett.* **837**, L20 (2017).

38. Srivastava, P. R., Chu, Y. J. L. & Swartzlander, G. A. Stable diffractive beam rider. *Opt. Lett.* **44**, 3082–3085 (2020).

39. Yu, N. & Capasso, F. Flat optics with designer metasurfaces. *Nat. Mater.* **13**, 139 (2014).

40. Siegel, J. et al. Self-stabilizing laser sails based on optical metasurfaces. *ACS Photo.* **6**, 2032–2040 (2019).

41. Ilic, O. & Atwater, H. A. Self-stabilizing photonic levitation and propulsion of nanostructured macroscopic objects. *Nat. Photo.* **13**, 289–295 (2019).

42. Salary, M. M. & Mosallaei, H. Photonic metasurfaces as relativistic light sails for doppler-broadened stable beam-riding and radiative cooling. *Laser Photo. Rev.* **14**, 1900311 (2020).

43. Evlyukhin, A. B., Matiushechkina, M., Zenin, V. A., Heurs, M. & Chichkov, B. N. Lightweight metasurface mirror of silicon nanosphere. *Opt. Mater. Express* **10**, 2706–2716 (2020).

44. Jin, W., Li, W., Orenstein, M. & Fan, S. Inverse design of lightweight broadband reflector for relativistic lightsail propulsion. *ACS Photo.* **7**, 2350–2355 (2020).

45. Gieseler, N., Rahimzadegan, A. & Rockstuhl, C. Self-stabilizing curved metasurfaces as a sail for light-propelled spacecrafts. *Opt. Express* **24**, 21562–21575 (2021).

46. Klessen, R. S. & Glover, S. C. Physical processes in the interstellar medium. In *Star Formation in Galaxy Evolution: Connecting Numerical Models to Reality*, 85–249 (Springer, 2016).

47. Draine, B. T. Physics of the interstellar and intergalactic medium, vol. 19 (Princeton University Press, 2010).

48. Hoang, T., Lazarian, A., Burkhart, B. & Loeb, A. The interaction of relativistic spacecrafts with the interstellar medium. *Astrophys. J.* **837**, 5 (2017).

49. Drobny, J. et al. Damage to Relativistic Interstellar Spacecraft by ISM Impact Gas Accumulation. *Am. Astr. Soc.* **908**, 248 (2021).

50. Drobny, J. et al. Survivability of metallic shields for relativistic spacecraft. *JBIS-J. Br. Interplanet Soc.* **73**, 446–456 (2020).

51. Wang, W., Roth, J., Lindig, S. & Wu, C. H. Blister formation of tungsten due to ion bombardment. *J. Nucl. Mater.* **299**, 124–131 (2001).

52. Pelizzo, M. et al. Stability of extreme ultraviolet multilayer coatings to low energy proton bombardment. *Opt. Express* **19**, 14838–14844 (2011).

53. Pelizzo, M. et al. Morphological and functional modifications of optical thin films for space applications irradiated with low-energy helium ions. *ACS Appl Mater. Interfaces* **10**, 34781–34791 (2018).

54. Livengood, R., Tan, S., Greenzweig, Y., Notte, J. & McVey, S. Subsurface damage from helium ions as a function of dose, beam energy, and dose rate. *J. Vac. Sci. Technol. B: Microelectron. Nanometer Struct. Process. Meas. Phenom.* **27**, 3244–3249 (2009).

55. Garoli, D. et al. Mirrors for space telescopes: Degradation issues. *Appl. Sci.* **10**, 7538 (2020).

56. Zuccon, S. et al. Effects of helium ion bombardment on metallic gold and iridium thin films. *Opt. Mater. Express* **5**, 176–187 (2015).

57. Pelizzo, M. G. et al. Dependence of the damage in optical metal/dielectric coatings on the energy of ions in irradiation experiments for space qualification. *Sci. Rep.* **11**, 1–12 (2021).

58. Yeh, P. & Hendry, M. Optical waves in layered media. *Phys. Today* **43**, 77 (1990).

59. Inc., C. Comsol multiphysics. https://www.comsol.com/ (2022).

60. Lucks, C., Deem, H. & Wood, W. *Thermal properties of six glasses and two graphites.* 39 (American Ceramic Society Bulletin US, 1960).

61. Scott, R. B. Cryogenic engineering (Books on Demand, 1959).

62. Van Vlack, L. H. Physical Ceramics for Engineers (1960).

63. Desai, P. D. Thermodynamic properties of iron and silicon. *J. Phys. Chem. Ref. Data* **15**, 967–983 (1986).

64. Kelley, K. K. *High-temperature heat-content, heat-capacity, and entropy data for inorganic compounds.* 476 (US Government Printing Office, 1949).

65. Tsou, C., Huang, Y.-S., Li, H.-C. & Lai, T.-H. Determination of thermal expansion coefficient of thermal oxide. *Sens. Mater.* **17**, 441–451 (2005).

66. Yang, C., Fan, H., Qiu, S., Xi, Y. & Chen, J. Effects of thermal expansion coefficient mismatch on structure and electrical properties of tio_2 film deposited on si substrate. *Surf. Rev. Lett.* **15**, 487–491 (2008).

Acknowledgements

Author contributions

G.S. developed the mathematical code and carried out all the simulations; he draft some parts of the paper. G.F. conceived the thermal analysis, contributed to simulations and draft some parts of the paper. A.J.C. coordinated the mathematical modeling, wrote the paper and contributed to its finalization. P.L. provided insightful ideas and inputs, as well as valuable feedback. R.R., M.B. and D.G. contributed with fruitful scientific discussions. M.G.P. conceived the paper scientific idea, coordinated the scientific activities and simulations, wrote the paper and finalize it. All authors reviewed the final manuscript.

Competing interests

The authors declare no competing interests.

Additional information

Supplementary information The online version contains supplementary material available at https://doi.org/10.1038/s43246-022-00240-8.

Correspondence and requests for materials should be addressed to Maria G. Pelizzo.

Peer review information *Communications Materials* thanks Ognjen Ilic and Elena Petrovna Popova for their contribution to the peer review of this work. Primary Handling Editors: Aldo Isidori. Peer reviewer reports are available.

Reprints and permission information is available at http://www.nature.com/reprints

Publisher's note Springer Nature remains neutral with regard to jurisdictional claims in published maps and institutional affiliations.